



# Simultaneous Design of Non-Newtonian Lubricant and Surface Texture Using Surrogate-Based Optimization

Yong Hoon Lee\*, Jonathon K. Schuh<sup>†</sup>, Randy H. Ewoldt<sup>‡</sup> and James T. Allison<sup>§</sup>  
*University of Illinois at Urbana-Champaign, Urbana, Illinois, 61801, USA*

Surface textures decrease friction in lubricated sliding contact with Newtonian lubricants. When using a non-Newtonian lubricant, the friction reduction is enhanced. In this study, we present a simultaneous design of the shape of a textured surface and the non-Newtonian viscometric functions using a multiobjective surrogate-based optimization technique. We model the flow of the non-Newtonian fluids between a flat plate and a texture surface using two different models: the Criminale-Ericksen-Filbey (CEF) model (which can be used to derive a modified Reynolds equation), and a multi-mode Giesekus model (which is used with the full 3-D Cauchy Momentum equations). We demonstrate the efficiency of our previously developed multiobjective adaptive surrogate modeling-based optimization (MO-ASMO) method, and provide insights into co-designing of the lubricant and textured surface, and how these results can be physically realized.

## I. Introduction

Surface textures decrease friction in lubricated sliding contact with Newtonian fluids.<sup>1–3</sup> We have previously shown that this friction reduction can be enhanced using more general surface topographies.<sup>4</sup> For that study, we developed surface parameterization techniques for generating an arbitrary texture profile subject to a limitation on the local slope (manufacturability constraint). We modeled the flow of an incompressible Newtonian fluid over the textured surfaces using the Reynolds equation,<sup>5</sup> and used this model to determine the optimal texture profile for minimizing frictional loss (shear stress) and maximizing load capacity (normal force).

We have also experimentally studied friction reduction with surface textures and viscoelastic non-Newtonian lubricants.<sup>6,7</sup> Viscoelastic non-Newtonian lubricants can decrease shear stress due to shear thinning and increase the load capacity due to normal stress differences. These additional fluid properties, when coupled with surface textures, result in greater friction reduction than when using surface textures or viscoelastic non-Newtonian lubricants independently.

Based on these observations, we extend our design study to include viscoelastic effects in friction reduction. We include viscoelastic effects through two different models: the Criminale-Ericksen-Filbey (CEF) model, and a multi-mode Giesekus model. The flow fields with both models are three dimensional; however, the CEF model is less computationally expensive because it can be used to derive a modified Reynolds equation,<sup>8</sup> whereas the multi-mode Giesekus model must be used with the full 3-D Cauchy Momentum equations. Combinations of the fluid models and governing equations are given in Table 1, and are discussed in more detail in Sect. II.A and III.A. We compare the results with the viscoelastic models to a Newtonian fluid reference case.

Figure 1 describes the design problem presented. We have adapted our previous design optimization strategy<sup>4,5</sup> to design both surface texture topography and non-Newtonian viscometric functions. Figure 1(a) shows the setup used previously in experiments;<sup>6</sup> the fluid is confined between a flat plate that rotates at a constant angular velocity and a stationary textured surface. A sector shown in Figs. 1(b)-(c) is an example

\*Graduate Student, Mechanical Science and Engineering, 104 S Mathews Ave, Urbana IL, 61801, AIAA Student Member

<sup>†</sup>Graduate Student, Mechanical Science and Engineering, 105 S Mathews Ave, Urbana IL, 61801

<sup>‡</sup>Associate Professor, Mechanical Science and Engineering, 105 S Mathews Ave, Urbana IL, 61801

<sup>§</sup>Assistant Professor, Industrial and Enterprise Systems Engineering, 104 S Mathews Ave, Urbana IL, 61801, AIAA Member

Table 1. Fluid models used for design in this study and corresponding solver governing equations.

Case no.	Fluid model	Governing equation	Dimension
1	Criminale-Ericksen-Filbey (CEF) model	Reynolds equation	2D ( $r, \theta$ )
2	Multi-mode Giesekus model	Cauchy momentum equation	3D ( $r, \theta, z$ )
0	Newtonian fluid	Cauchy momentum equation	3D ( $r, \theta, z$ )

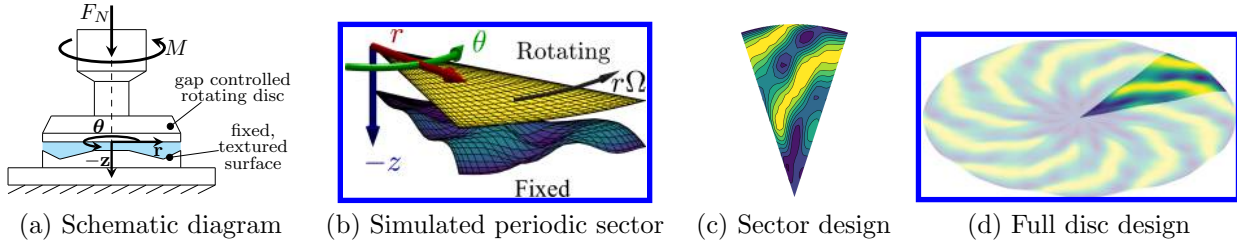


Figure 1. A lubricated periodic surface texture design problem in a rotational tribo-rheometer setting.

design of the surface texture height profiles as a function of  $r$  and  $\theta$ . Figure 1(d) shows an example of a fully-textured disc using 10 periodic sectors.

As we extend our study to include nonlinear viscoelastic models, and move from 2-D to 3-D, the computational cost associated with the design problem increases significantly. In our previous study, where we modeled the fluid flow with the Reynolds equation, the computational cost of the optimization was reduced by using a coarse design mesh that was mapped onto a finer analysis mesh.<sup>4</sup> The computational cost of the optimization can also be reduced by linearizing the Reynolds equation (with respect to the design variables) and iteratively solving using a sequential linear programming (SLP) algorithm.<sup>9</sup> Here, we solve the full nonlinear optimization problem using surrogate modeling. We have developed a multiobjective adaptive surrogate modeling-based optimization (MO-ASMO) strategy<sup>10</sup> that uses efficient sampling strategies to explore a constrained design space and search for Pareto-optimal solutions. This algorithm is developed specifically for problems with narrow or geometrically complex feasible design domains. We have imposed a local slope constraint on the gap height profile (manufacturability constraint), and have constrained the viscometric functions to represent realizable materials. It is demonstrated that the MO-ASMO algorithm is beneficial by reducing the overall computational cost of the combined fluid and texture design optimization problem.

## II. Formulation

### II.A. Non-Newtonian Fluid Models

Non-Newtonian fluids show different rheological behavior than Newtonian fluids; the behaviors most often studied are shear thinning, viscoelasticity, generation of normal stresses in shear, and extensional thickening. These rheological behaviors can be described using different constitutive models. Here, we model the non-Newtonian fluids using two different models: the Criminale-Ericksen-Filbey (CEF) model and the multi-mode Giesekus model.

#### II.A.1. Criminale-Ericksen-Filbey (CEF) Model

The Criminale-Ericksen-Filbey (CEF) model<sup>11,12</sup> is a constitutive model for the stress tensor  $\underline{\underline{\tau}}$  that contains terms for the shear-rate dependent viscosity and the first and second normal stress differences, and is given as:

$$\underline{\underline{\tau}} = \eta(\dot{\gamma}) \underline{\underline{\gamma}}_{(1)} - \frac{1}{2} \Psi_1(\dot{\gamma}) \underline{\underline{\gamma}}_{(2)} + \Psi_2(\dot{\gamma}) \left( \underline{\underline{\gamma}}_{(1)} \cdot \underline{\underline{\gamma}}_{(1)} \right), \quad (1)$$

Table 2. Parameters for each fluid model used in design studies.

Case no.	$N_\phi$	$n_r$	$n_\theta$	$n_z$	$\Omega$ [rad/s]	$\eta_s$ [Pa·s]	$\rho_s$ [kg/m <sup>3</sup> ]	$n_{\text{mode}}$	$\theta_{\text{incl}}$ [°]
0	10	6	6	4	10.0	$9.624 \times 10^{-3}$	873.4	0	60.0
1	10	6	6	-	10.0	$9.624 \times 10^{-3}$	873.4	2	60.0
2	10	6	6	4	10.0	$9.624 \times 10^{-3}$	873.4	2	60.0

where the upper convective time derivative<sup>13</sup> of the shear rate  $\underline{\dot{\gamma}}$  is defined as:

$$\underline{\underline{\gamma}}_{(1)} = \underline{\dot{\gamma}}, \quad \text{and} \quad \underline{\underline{\gamma}}_{(n+1)} = \frac{\partial \underline{\underline{\gamma}}_{(n)}}{\partial t} + (\mathbf{u} \cdot \nabla) \underline{\underline{\gamma}}_{(n)} - \left( (\nabla \mathbf{u})^T \cdot \underline{\underline{\gamma}}_{(n)} + \underline{\underline{\gamma}}_{(n)} \cdot (\nabla \mathbf{u})^T \right). \quad (2)$$

The viscometric functions in this constitutive model,  $\eta$ ,  $\Psi_1$ , and  $\Psi_2$ , are functions of the shear rate  $\dot{\gamma}$  where  $\dot{\gamma} = \sqrt{\frac{1}{2} \underline{\dot{\gamma}} : \underline{\dot{\gamma}}}$ . The first term in Eqn. (1) models a generalized Newtonian fluid, and the remaining terms model the behavior of elastic effects from normal stress differences.

### II.A.2. Multi-Mode Giesekus Model

The CEF model cannot predict transient effects on the shear stress tensor  $\underline{\underline{\tau}}$ . To capture the contributions of possible transient effects on the friction reduction, we need to use a more general constitutive equation that includes time derivatives of the shear stress. Here, we choose a multi-mode Giesekus model to simulate our polymeric stresses, given as:

$$\lambda_i \left( \frac{\partial \underline{\underline{\tau}}_{p_i}}{\partial t} + (\mathbf{u} \cdot \nabla) \underline{\underline{\tau}}_{p_i} - \left[ (\nabla \mathbf{u})^T \cdot \underline{\underline{\tau}}_{p_i} + \underline{\underline{\tau}}_{p_i} \cdot (\nabla \mathbf{u}) \right] \right) + \underline{\underline{\tau}}_{p_i} + \frac{\lambda_i \alpha_i}{\eta_{p_i}} \left( \underline{\underline{\tau}}_{p_i} \cdot \underline{\underline{\tau}}_{p_i} \right) = \eta_{p_i} \underline{\dot{\gamma}}, \quad (3)$$

where  $\lambda_i$  is the relaxation time,  $\eta_{p_i}$  is the polymeric viscosity, and  $\alpha_i$  is the mobility factor of the  $i$ th-mode. The contributions from each mode are assumed to be additive such that:

$$\underline{\underline{\tau}}_p = \sum_{i=1}^{n_{\text{mode}}} \underline{\underline{\tau}}_{p_i}. \quad (4)$$

### II.A.3. Parameters

Fluid properties, model parameters, computational mesh resolutions, operating conditions, and design constraint parameters for all the cases are listed in Table 2. Number of periodic sectors to construct a full disc is denoted by  $N_\phi$ . Number of mesh nodes for each  $r$ -,  $\theta$ -, and  $z$ -direction corresponds to  $n_r$ ,  $n_\theta$ , and  $n_z$ .  $\Omega$  denotes the angular velocity of the flat plate as shown in Figure 1(a);  $\eta_s$  and  $\rho_s$  denote the solvent viscosity and density.  $n_{\text{mode}}$  denotes the number of modes for the Giesekus model, and  $\theta_{\text{incl}}$  denotes the maximum angle for the texture inclination explained in Sect. II.B.

## II.B. Design Problem Formulation

The design problem considered here is simultaneously minimizing the input power to the rotating flat plate and maximizing the load-supporting normal force, while constraining the maximum texture inclination angle. This problem is formulated as a constrained nonlinear optimization problem in negative null form:

$$\underset{\mathbf{x}_{\text{lb}} \leq \mathbf{x} \leq \mathbf{x}_{\text{ub}}}{\text{minimize}} \quad \mathbf{f}(\mathbf{x}) = [P, -F_N] \quad (5a)$$

$$\text{subject to} \quad \mathbf{g}_{\text{geom, incl}}(\mathbf{x}) = \left[ \left\{ \left| \frac{h_{ij} - h_{(i-1)j}}{r_i - r_{(i-1)}} \right| : \begin{array}{l} i = 2, \dots, n_r \\ j = 1, \dots, n_\theta \end{array} \right\}, \right. \\ \left. \left\{ \left| \frac{h_{ij} - h_{i(j-1)}}{r_i \theta_j - r_i \theta_{(j-1)}} \right| : \begin{array}{l} i = 1, \dots, n_r \\ j = 2, \dots, n_\theta \end{array} \right\} \right] - \theta_{\text{incl}} \leq \mathbf{0} \quad (5b)$$

$$\mathbf{g}_{\text{geom,lowpt}}(\mathbf{x}) = \{-h_{1n_r} + h_{in_r} : i = 2, \dots, n_\theta\} \leq \mathbf{0} \quad (5c)$$

$$\mathbf{h}_{\text{geom,bc}}(\mathbf{x}) = \{h_{i1} - h_{in_\theta} : i = 1, \dots, n_r\} = \mathbf{0}, \quad (5d)$$

where:

$$P = M\Omega \quad (6a)$$

$$F_N = N_\phi \int_{-\varphi/2}^{\varphi/2} \int_{R_i}^{R_o} (p|_{z=0} - \tau_{zz}|_{z=0}) r dr d\theta \quad (6b)$$

$$M = N_\phi \int_{-\varphi/2}^{\varphi/2} \int_{R_i}^{R_o} (r\tau_{\theta z}|_{z=0}) r dr d\theta \quad (6c)$$

$$p_{ij}, \underline{\tau}_{ij} \leftarrow \text{flow-solver}(\mathbf{x}), \quad (6d)$$

and  $\theta_{\text{incl}}$  is the maximum allowable local inclination angle between neighboring control points of the Lagrange polynomial interpolation over the texture geometry. The design objectives are to minimize the power input  $P = M\Omega$  and to maximize the normal force  $F_N$  simultaneously. Simultaneous optimization of the two objective functions (multiobjective optimization) results in a set of Pareto-optimal (non-dominated) solutions. The design variable vector  $\mathbf{x}$  is comprised of both surface height values at mesh nodes, and fluid model parameters:

$$\mathbf{x} = [\{h_{ij} : i = 1, \dots, n_r, j = 1, \dots, n_\theta\}, \{\lambda_k, \alpha_k, \eta_{pk} : k = 1, \dots, n_{\text{mode}}\}], \quad (7)$$

assuming we have a given fluid viscosity  $\eta$ , used as  $\eta(\dot{\gamma}_1 \approx 0) = \eta$  and  $\eta_s = \eta$  for the Giesekus model. The viscometric functions for the CEF model can be described using analytical solutions for those values from other models; for example, the Giesekus model in steady simple shear flow has analytical expressions for  $\eta$  and  $\Psi_1$  that depends on the same parameters we use for the full Giesekus model solver ( $\eta_p$ ,  $\lambda$ , and  $\alpha$ ). This treatment reduces the number of design variables significantly and allows us to use the same design variable set for the two fluid models. A manufacturability constraint applied in our previous study<sup>4</sup> is also implemented via the first vector-valued inequality constraint function  $\mathbf{g}_{\text{geom}}(\cdot)$ . The inclination angle between the surface mesh nodes is limited to a predefined maximum value. Also, material functions used in the non-Newtonian fluid models are constrained to disallow certain shapes that are not physically realizable.

### III. Methodology

#### III.A. Solution Procedures for Fluid Flow

##### III.A.1. Reynolds Equation With CEF Model

Previously we have developed code for solving the flow of an incompressible Newtonian fluid over general surface textures using the Reynolds equation,<sup>5</sup> and have used that code for optimization of textured surfaces.<sup>4</sup> A previous study<sup>8</sup> showed that viscoelasticity can be included in the thin film governing equations using the CEF model. Here we derive a modified Reynolds equation with the CEF model for our design problem by applying the following assumptions: *i*) the gap height is small compared to the radius of the textured disk ( $h(r, \theta)/R \ll 1$ ), *ii*) shear rate ( $\dot{\gamma}(r, \theta) = r\Omega/h(r, \theta)$ ) is independent of  $z$ , *iii*)  $\exists$  no second normal stress difference coefficient ( $\Psi_2 = 0$ ), resulting in pressure that does not vary in the  $z$  direction ( $\partial p/\partial z = 0$ ), and *iv*) zero gradients in  $z$  direction are assumed for the other viscometric functions ( $\partial\eta/\partial z = 0$ ,  $\partial\Psi_1/\partial z = 0$ ). Splitting the pressure and velocity fields into  $p = p_0 + p_1$  and  $\underline{u} = \underline{u}_0 + \underline{u}_1$ , and applying appropriate Dirichlet boundary conditions for the velocity fields results in two equations governing the flow of a CEF fluid over general surface textures; an equation similar to the steady state Reynolds equation given as

$$\frac{1}{r} \frac{\partial}{\partial r} \left( \frac{rh^3}{12\eta} \frac{\partial p_0}{\partial r} \right) + \frac{1}{r} \frac{\partial}{\partial \theta} \left( \frac{h^3}{12\eta r} \frac{\partial p_0}{\partial \theta} \right) = \frac{1}{r} \frac{\partial}{\partial \theta} \left( \frac{r\Omega h}{2} \right), \quad (8)$$

which includes shear thinning, and a modified Reynolds equation (where the right hand side depends on the local Reynolds number and local relationship between elasticity and viscosity) given as

$$\frac{1}{r} \frac{\partial}{\partial r} \left( \frac{rh^3}{12\eta} \frac{\partial p_1}{\partial r} \right) + \frac{1}{r} \frac{\partial}{\partial \theta} \left( \frac{h^3}{12\eta r} \frac{\partial p_1}{\partial \theta} \right) = \frac{1}{r} \frac{\partial}{\partial r} (rG_r) + \frac{1}{r} \frac{\partial}{\partial \theta} (G_\theta) \quad (9)$$

where

$$G_r = \frac{r\Omega h}{40} \left( \frac{\rho\Omega h^2}{\eta} \right) B_r + \frac{r\Omega h}{12} \left( \frac{\Psi_1\Omega}{\eta} \right) A_r \quad (10a)$$

$$B_r = 1 - \frac{1}{3} \left( \frac{1}{\eta\Omega} \frac{\partial p_0}{\partial \theta} \left( \frac{h}{r} \right)^2 \right) + \frac{1}{28} \left( \frac{1}{\eta\Omega} \frac{\partial p_0}{\partial \theta} \left( \frac{h}{r} \right)^2 \right)^2 \quad (10b)$$

$$A_r = -1 - \frac{1}{20} \left( \frac{1}{\eta\Omega} \frac{\partial p_0}{\partial \theta} \left( \frac{h}{r} \right)^2 \right)^2 + \frac{1}{20} \left( \frac{1}{\eta\Omega} r \frac{\partial p_0}{\partial r} \left( \frac{h}{r} \right)^2 \right)^2 \quad (10c)$$

$$G_\theta = \frac{r\Omega h}{240} \left( \frac{\rho\Omega h^2}{\eta} \right) B_\theta + \frac{r\Omega h}{120} \left( \frac{\Psi_1\Omega}{\eta} \right) A_\theta \quad (10d)$$

$$B_\theta = \left( \frac{1}{\eta\Omega} r \frac{\partial p_0}{\partial r} \left( \frac{h}{r} \right)^2 \right) - \frac{3}{14} \left( \frac{1}{(\eta\Omega)^2} r \frac{\partial p_0}{\partial r} \frac{\partial p_0}{\partial \theta} \left( \frac{h}{r} \right)^4 \right) \quad (10e)$$

$$A_\theta = \left( \frac{1}{(\eta\Omega)^2} r \frac{\partial p_0}{\partial r} \frac{\partial p_0}{\partial \theta} \left( \frac{h}{r} \right)^4 \right). \quad (10f)$$

We solve these equations using a Galerkin pseudospectral method for a periodic sector with  $p_0|_{r=R_0} = p_1|_{r=R_0} = 0$ ,  $\partial p_0/\partial r|_{r=R_i} = \partial p_1/\partial r|_{r=R_i} = 0$ , and periodic boundary conditions in the  $\theta$  direction. The Dirichlet boundary condition  $p|_{r=R_0} = 0$  is used to match results obtained by Macosko<sup>14</sup> for flow between parallel disks.

### III.A.2. Cauchy Momentum Equation Solver With Multi-Mode Giesekus Model

The Cauchy momentum equation is written in tensorial form as:

$$\frac{\partial \underline{u}}{\partial t} + (\underline{u} \cdot \nabla) \underline{u} = -\frac{1}{\rho} \nabla p + \frac{\eta_s}{\rho} \nabla^2 \underline{u} + \frac{1}{\rho} \nabla \cdot \underline{\underline{\tau}}_p, \quad (11)$$

where  $\rho$  is the fluid density,  $\eta_s$  is the solvent viscosity, and  $\underline{\underline{\tau}}_p$  is the polymeric contribution to the shear stress. The contribution of the solvent has been pulled out of the stress tensor to help with stability.<sup>15</sup> We assume that the flow is incompressible ( $\nabla \cdot \underline{u} = 0$ ), and that the solvent and polymeric stresses add to produce the total shear stress:

$$\underline{\underline{\tau}} = \underline{\underline{\tau}}_s + \underline{\underline{\tau}}_p, \quad \underline{\underline{\tau}}_s = \eta_s \dot{\underline{\underline{\gamma}}}. \quad (12)$$

The above equations (conservation of momentum and incompressibility) provide four equations with ten unknowns; therefore, a constitutive equation must be used for  $\underline{\underline{\tau}}_p$  to solve the fluid flow system. As stated above, we are using the multi-mode Giesekus model given in Eqn. 3 with  $n_{\text{mode}} = 2$ .

We solve the transient governing equations in cylindrical coordinates to steady state. The equations are solved on a periodic sector of a disk where  $z \in [-h(r, \theta), 0]$ ; this is similar to our previous solution method with the Reynolds equation.<sup>4,5</sup> The equations are discretized in space using a Galerkin pseudospectral method (where we have mapped our 3-D periodic sector onto the  $[-1, 1]$  cube using an invertible mapping,<sup>16,17</sup> where it was assumed that the gradient of the gap height  $h(r, \theta)$  exists everywhere in the computational domain), and are discretized in time using a third-order Adams Bashforth time stepper with third-order extrapolation for the nonlinear terms. A velocity splitting technique is used for solving the pressure Poisson equation at each time step, and the diffusion terms are treated implicitly to aid stability.<sup>15</sup>

The transient Cauchy momentum equations are solved with maximum CFL number of 0.8, where local CFL condition is defined as  $C = \underline{u}\Delta t/\Delta x$ . Each fluid parameter has its own bound constrained by physical or numerical limitations. For example, the mobility factor  $\alpha_i$  is bounded between 0.01 and 0.50. When the  $\alpha_i$  decreased smaller than 0.01, increased Weissenberg number causes numerical instability and the computation tends to break down.<sup>18</sup>

### III.B. Design Procedures

#### III.B.1. Texture Design Representation

We chose a pseudospectral method for both fluid models given in Sect. III.A.1 and III.A.2, which assumes the computational grid to be approximated by Lagrange polynomials of  $N_D$ -th order for each geometric dimension  $D$ .<sup>19</sup> The texture design given to the flow simulation is represented by the gap height  $h_{ij}$  for  $i, j = 1, \dots, n_r$ , and the solution procedure of the pseudospectral method assumes that the entire computational domain is continuous and smooth in Lagrange polynomial form. Thus, we could get very accurate fluid flow solution even with a very small number of grid points over each direction. Solutions for the design problem will also be smooth and continuous in the form of Lagrange polynomial. By maintaining the same mesh for the design representation and the simulation domain representation, we can get very accurate design solutions without requiring a large number of design variables due to the characteristics of the interpolating polynomials used in the pseudospectral method.

#### III.B.2. Multiobjective Adaptive Surrogate Modeling-Based Optimization (MO-ASMO)

The multiobjective adaptive surrogate modeling-based optimization (MO-ASMO)<sup>10</sup> is a surrogate-based optimization framework that can handle multiple objective functions, tens or hundreds of design variables, and multiple linear and nonlinear constraints. Figure 2 briefly illustrates a general structure of this type of algorithm (direct sampling<sup>20</sup>). We have developed this method primarily for solving problems with complicated constraints that result in narrow or otherwise difficult to navigate feasible domains. It avoids infeasible samples to reduce inefficient use of high-fidelity simulations. The method aims to balance choosing samples that help improve surrogate model accuracy in the vicinity of the Pareto-optimal solution (a hypersurface in the design space), with choosing samples that aid exploration to improve the probability of finding global optima. The problem considered here is well-matched for this MO-ASMO method as it involves a large number of constraints that interrelate multiple design variables, and a computationally expensive simulation. Readers are referred to Ref. 10 for a detailed description of this method, including sampling and validation, as well as openly-available source code.

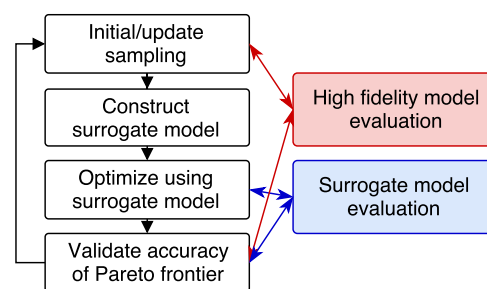


Figure 2. Flow chart illustrating the MO-ASMO framework with direct sampling method.<sup>10,20</sup>

## IV. Results and Discussion

### IV.A. Case 1: CEF Model Case Result

Solutions of design problem case 1 (CEF model with Reynolds equation) are illustrated in the objective function space in Fig. 3. Since the objective functions are *i*) to minimize the power input and *ii*) to maximize the normal force, we desire points in this space to be close to the top-left corner. Optimal solutions (in the form of a Pareto frontier) are marked with colored circles, while all the explored designs are marked with black and gray-scale dots. Design points marked as black or darker gray dominate design points marked as lighter gray. Points having the same gray-scale intensity means they have the same rank according to a non-dominated sorting strategy.<sup>21</sup> Optimal solutions have a range of input power values from  $4.31 \times 10^{-4}$  to  $3.56 \times 10^{-3}$  [W], and a range of normal force values from  $6.16 \times 10^{-4}$  to  $1.50 \times 10^{-1}$  [N]. The labels (a) through (f) that identify specific marked points in Fig. 3 correspond to the texture and fluid designs given in Fig. 4(a)-(f).

Design result (a) for case 1 (refer to point (a) in Figs. 3 and 4(a)) is an anchor point of the Pareto set in the objective function space; it has the minimum power value over all feasible designs. An anchor point is a non-dominated point with one of the objective functions optimized, with all other objective functions ignored. Here point (a) results when power is minimized and normal force is not considered. This minimum-power design exhibits a relatively flat texture surface with a small amount of asymmetry, and does not generate much normal force ( $4.31 \times 10^{-4}$  [N]). This design solution includes no non-Newtonian fluid properties, since the polymer viscosity values have converged to zero for all modes.

Design result (f) (refer to point (f) in Figs. 3 and 4(f)) is the other anchor point, which has a maximum

normal force without consideration of power input. Unlike the former anchor point, this design has strong asymmetry with distinct elevation changes in the texture to form a spiral blade-like shape. As explained in our previous study, this spiral texture design directs the fluid pressure radially inward by acting as a converging channel, eventually generating the positive net normal force due to increased pressure near the disc center.<sup>4</sup> Also, this design solution includes non-Newtonian fluid properties with high polymer viscosity values for both modes ( $\eta_{p1}$  and  $\eta_{p2}$ ). These results are congruent with earlier studies based on Newtonian fluids where it was observed that: *i*) a deeper surface reduces frictional loss, *ii*) symmetric surfaces do not generate any normal force due to geometric properties, and *iii*) stronger asymmetry generates larger normal forces.<sup>4,5</sup>

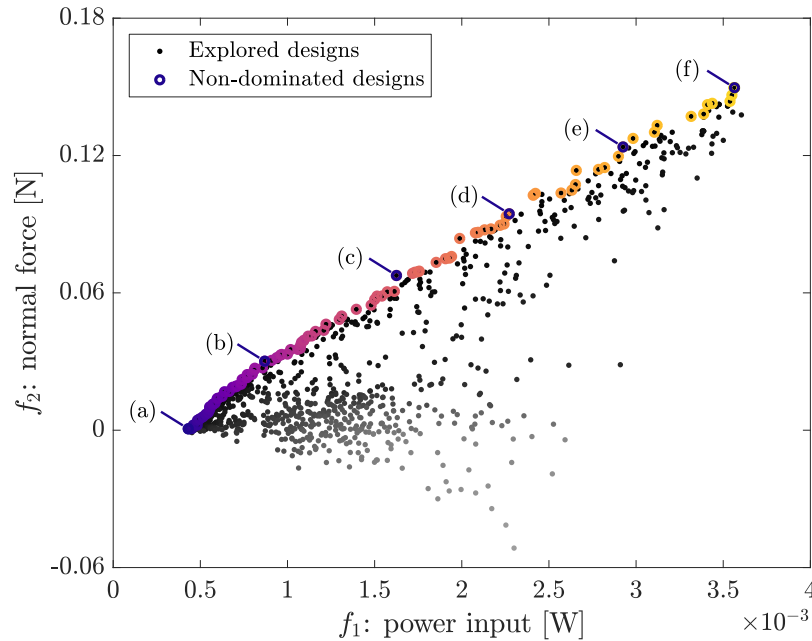


**Figure 3. Explored designs and optimal solutions (non-dominated designs) for the CEF model case in the objective function space.**

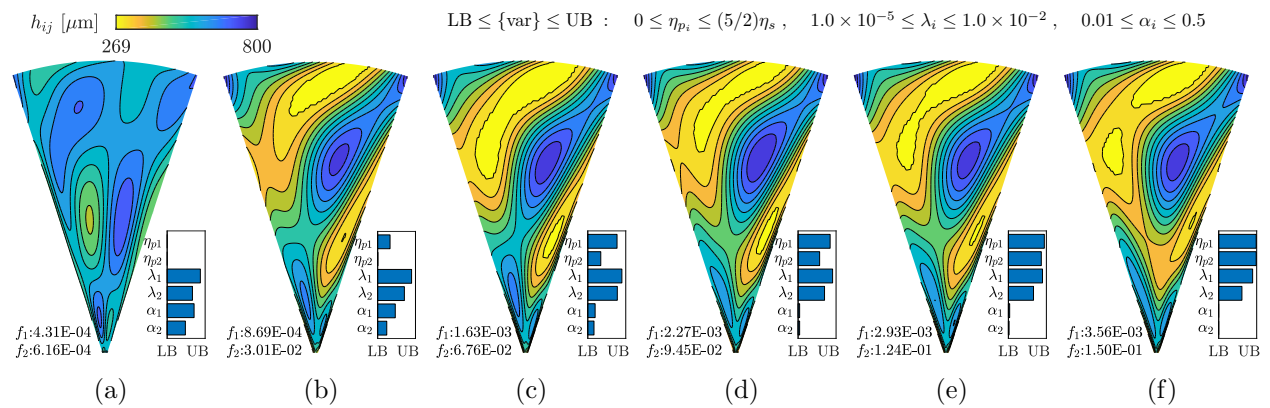


**Figure 4. Sample textured sector and fluid designs in the Pareto set from the CEF model case.**

Other designs on the Pareto frontier between these two anchor points (refer to points (b)-(e) in Figs. 3 and 4(b)-(e)) have consistent trends. Specifically, we observe that: *i*) the general shape of the surface texture designs does not change significantly, but steeper inclines in the texture are required to generate higher normal forces, and *ii*) an increased polymer viscosity and a decreased nonlinearity (anisotropy described by the mobility factor) help obtain higher normal forces. These results show that the nonlinearity mainly plays a role when we optimize both objective functions simultaneously. An increased polymer viscosity tends to help increase load capacity, and increased nonlinearity helps reduce frictional losses. It should be noted that

these responses are non-monotonic and have optimum values for achieving a certain balance between the two objectives.

#### IV.B. Case 2: Multi-Mode Giesekus Model Case Result

Solutions of the design problem case 2 (multi-mode Giesekus model with transient Cauchy momentum equation) are illustrated in the objective function space in Fig. 5. As with the CEF model (Fig. 3), the direction of desired performance is toward the top-left corner, and the labeling strategy is kept consistent. Optimal solutions have a range of power input from  $3.77 \times 10^{-4}$  to  $2.56 \times 10^{-3}$  [W], and a normal force range of  $2.11 \times 10^{-4}$  to  $9.01 \times 10^{-2}$  [N]. The labels (a) through (f) indicate specific non-dominated points in Fig. 5 that correspond to the texture and fluid designs shown in Fig. 6(a)-(f).

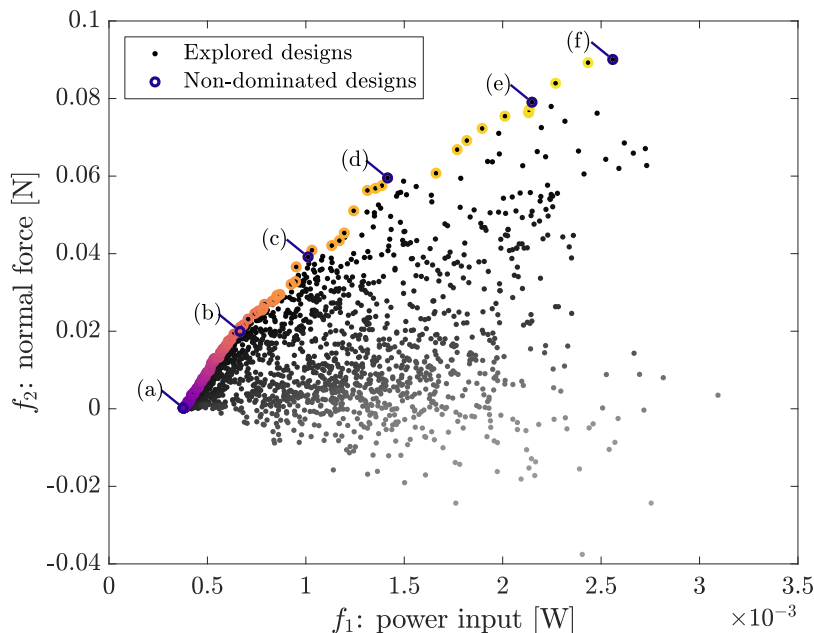


Figure 5. Explored designs and optimal solutions (non-dominated designs) for the multi-mode Giesekus model case in the objective function space.

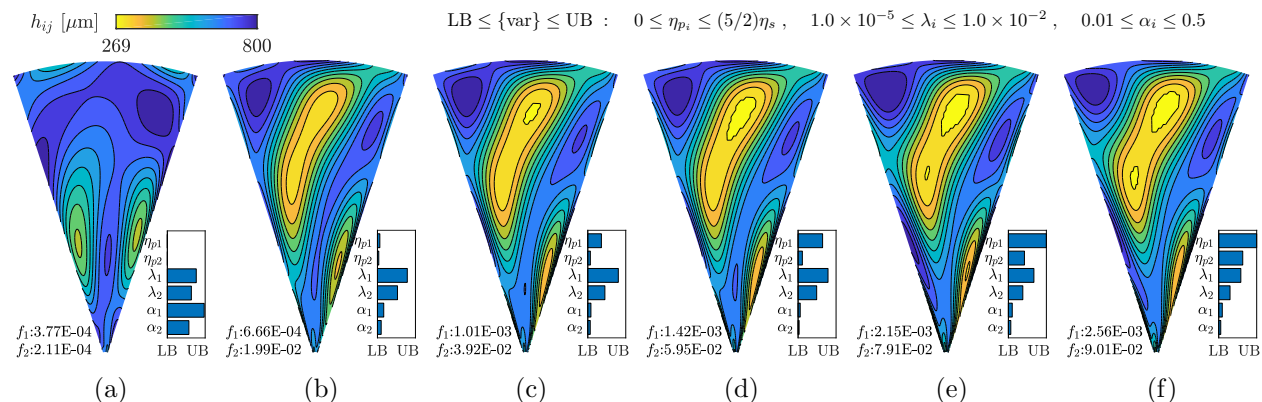


Figure 6. Sample textured sector and fluid designs in the Pareto set from the multi-mode Giesekus model case.

Design (a) of case 2 (refer to point (a) in Figs. 5 and 6(a)) is the anchor point with minimum power input. This design shows a relatively flat texture surface with a small amount of asymmetry and Newtonian fluid properties, as was observed in case 1. The maximum normal force anchor point is design point (f) in Fig. 5 (also in Fig. 6(f)). This design has the most distinct elevation changes in the texture, and, similar to the previous case, forms a spiral blade-like shape.

Other designs on the Pareto frontier between these two anchor points (refer to points (b)-(e) in Fig. 5 and Fig. 6(b)-(e)) also exhibit consistent trends: *i*) the surface texture shapes do not change significantly, but larger elevation changes are needed to acquire higher normal forces, and *ii*) an increased polymer viscosity is associated with higher normal forces, and *iii*) the nonlinearity (mobility factor) is maintained with low (but non-zero) values for entire range of designs. Thus, for case 2, we can observe an increase in the normal force with a simultaneous increase in the power input as polymer viscosity values in modes 1 and 2 increase (from design (b) through (f)). However, all the optimal solutions converged to low mobility factor values, suggesting that shear thinning is not desirable. Also, the optimal textures from case 2 are in general deeper than those for case 1.

#### IV.C. Case 0: Newtonian Fluid Model Case Result

An additional study is performed here using a Newtonian fluid model with transient Cauchy momentum equation to provide a reference solution (case 0). Solutions of this case are shown in Fig. 7. Optimal solutions have a range of power input from  $3.43 \times 10^{-4}$  to  $6.73 \times 10^{-4}$  [W], and a range of normal force values from  $1.45 \times 10^{-4}$  to  $2.51 \times 10^{-2}$  [N]. The labels (a) through (f) indicating specific marked points in Fig. 7 correspond to the texture and fluid designs given in Fig. 8(a)-(f).

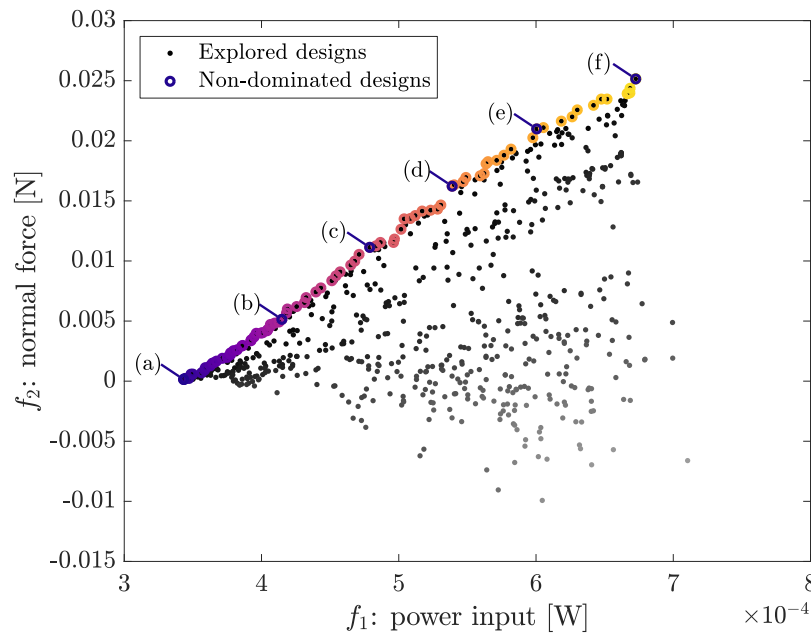


Figure 7. Explored designs and optimal solutions (non-dominated designs) for the Newtonian fluid model case in the objective function space.

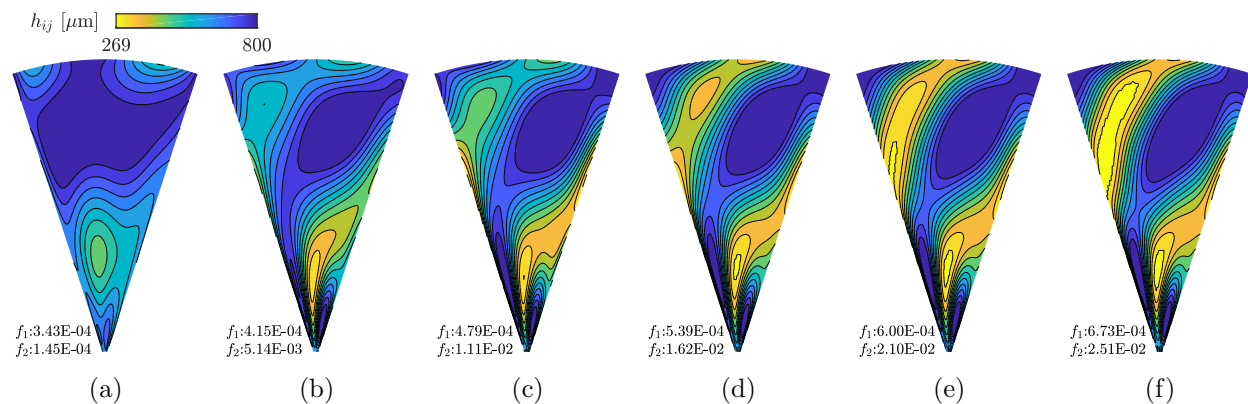


Figure 8. Sample textured sector designs in the Pareto set from the Newtonian fluid model case.

Similar to the results obtained from the non-Newtonian fluid studies, we see similar trends in the shape of the surface textures. An anchor point with a minimum power input (shown as design (a) of case 0) has a deep and relatively planar textured surface. The maximum normal force anchor point, shown as design (f), has a sharp and distinct asymmetric spiral blade-like texture shape, which directs the fluid pressure radially inward to generate a positive net normal force.

Other designs on the Pareto frontier between these two anchor points (refer points (b)-(e) in Fig. 7 and Fig. 8(b)-(e)) have a consistent trend; unlike the other two non-Newtonian fluid cases, the texture designs are notably different to each other. The optimal designs on the Pareto frontier in this case show how changes in texture design purely affect changes in generated normal force values since all the designs have the same Newtonian fluid properties. Comparatively sudden elevation changes in the texture are observed for entire design points that generate normal forces (specifically see points (b)-(f)).

#### IV.D. Comparisons and Discussion

##### IV.D.1. Pareto Set Comparison

Figure 9 shows Pareto sets for three design studies simultaneously, including CEF (case 1), Giesekus (case 2), and Newtonian fluid model (case 0) studies. Colored dots represent Pareto-optimal solutions (design points) in the objective function space, while colored circles represent the corresponding utopia points for each of the three design studies.

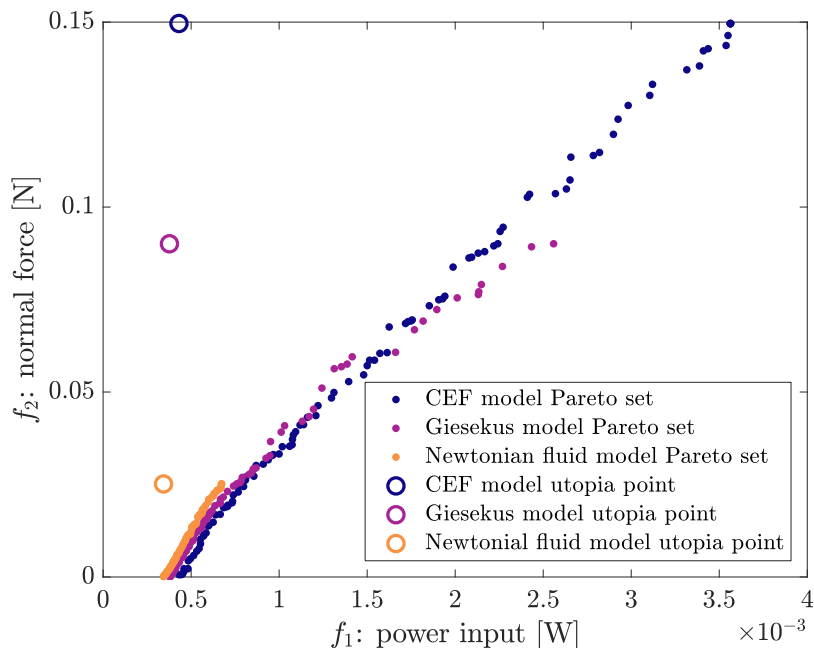


Figure 9. A comparison of the optimal solutions (Pareto set) of CEF, Giesekus, and Newtonian fluid models in the objective function space.

The study based on the Newtonian fluid model serves as a reference, illustrating how much normal force can be generated through improved texture design alone without tailoring non-Newtonian effects. For Newtonian fluids, Pareto-optimal designs span only a small range of power input levels (from  $3.43 \times 10^{-4}$  to  $6.73 \times 10^{-4}$  [W]). The maximum possible normal force generated without aid from viscoelastic effects is  $2.51 \times 10^{-2}$  [N].

When parameters that define fluid properties are added as design variables, the maximum possible normal force generated is increased by a factor of six. The CEF model case exhibits a maximum possible normal force of  $1.50 \times 10^{-1}$  [N], with a corresponding power input of  $3.56 \times 10^{-3}$  [W]. Using the multi-mode Giesekus model, we can obtain a maximum normal force of  $9.01 \times 10^{-2}$  [N], with a corresponding power input of  $2.56 \times 10^{-3}$  [W]. Although we used the same parameterizations for designing fluids in both non-Newtonian fluid cases, we see a significant difference in normal force generating capability. Design based on more simplified fluid simulations (i.e., modified Reynolds equation using a CEF fluid model) could explore designs that generate higher normal force values.

#### IV.D.2. Model Comparison

Based on the above results, the two fundamental problem types are: *i*) simultaneous design of texture and fluid properties, and *ii*) design of texture-only with fixed fluid properties. While the simultaneous texture and fluid design problem was solved using two distinct numerical fluid simulation models, they correspond to the same physical design problem. Both cases involve using a viscoelastic fluid (polymeric solution) as the lubricant, designing the fluid properties, and designing the texture shape. The only difference between these two cases is how behavior was predicted, and simplifying assumptions made. We highlight this point to clarify that the decision between methods can instead be made based on the following criteria: *i*) computational efficiency, *ii*) prediction accuracy, *iii*) range of numerical limits, and *iv*) range of types of fluid behaviors that the model can predict. The models are compared here along these dimensions.

First, the modified Reynolds equation with the CEF model has a very efficient computational structure; the entire optimization using the MO-ASMO algorithm took only 29 minutes using a dual Xeon X5650 workstation with 24-cores. The steady state solution can be obtained directly without using a time marching transient solution procedure. Also, the modified Reynolds equation can predict the pressure and stress of the flow field efficiently within assumptions made during derivation. Since the CEF model can include shear-rate dependent viscosity and normal stress differences in calculating the velocity and pressure fields, the nonlinear viscoelasticity observed in our polymeric lubricant can be predicted well. However, because of the assumptions and limitations underlying the Reynolds equation (described in Refs.<sup>4,5</sup>), prediction accuracy may be poor when certain flow conditions are present, such as recirculation or flow with non-trivial inertial effects. By looking at the solution, however, the case with the CEF model provides the greatest freedom in design exploration; it produces the highest normal force, although this model does have certain limitations. Also, within the design ranges of the other models (power input up to 2.5 [W] and normal force up to 0.1 [N]), this model could provide a mostly overlapping Pareto frontier when comparing to the Pareto frontiers produced using the other models.

Second, the Cauchy momentum equation with a multi-mode Giesekus model is the most computationally expensive choice, but it can predict the fluid flow very accurately, including inertial effects, recirculation, and other 3D effects. The Giesekus model can also include shear-rate dependent viscosity and normal stress difference effects on the velocity and pressure fields. Thus, this model is the most ideal for complex flow phenomena with nonlinear viscoelasticity. However, due to numerical instability under certain conditions, a particular set of input (shape and fluid) parameter values cannot be evaluated with this solver. Our MO-ASMO algorithm can handle these “unable-to-get-result” points by utilizing feasible region management functions based on a support vector domain description (SVDD) strategy. Thus, we improved efficiency by avoiding training samples that were incompatible with the model. After addressing this issue, the MO-ASMO algorithm produced improved solutions. However, even with efficient MO-ASMO algorithm, the computation time for this optimization problem was significant (31 hours using the same machine). The Pareto frontier for this case overlaps with the CEF model results, but it could not produce designs with high normal force generation.

#### IV.D.3. Texture Shape Comparison

Sample texture shapes of full discs from our design solutions are compared in Fig. 10. Texture designs from the CEF model case are shown in subfigures (a), (d), and (g); texture designs from the Giesekus model case are shown in subfigures (b), (e), and (h); texture designs from the Newtonian fluid model case are shown in subfigures (c) and (f). Sample textures given here are selected to compare the resulting optimal textures between different fluid model cases.

Designs are arranged such that the normal forces generated by each design in a given row is similar. The first row designs ((a), (b), and (c)) are the textures that generate normal forces on the order of  $1 \times 10^{-4}$  [N]. These surface texture designs are relatively flat with a limited amount of asymmetry. The second row designs ((d), (e), and (f)) are the textures that generate normal forces on the order of  $2 \times 10^{-2}$  [N]. These surface texture designs have very sharp and large elevation changes to create a spiral blade-like pattern as discussed in Sect. IV.A to IV.C. For the Newtonian fluid model case, which relies on the texture to generate a normal force, the resulting design ((f)) generates a normal force value close to the highest possible without non-Newtonian fluid behavior. The third row ((g) and (h)) are the textures that generate normal forces on the order of  $1 \times 10^{-1}$  [N], and are the highest normal force values for each of the respective design problems. Texture designs are not significantly different from the designs in the second row. This observation indicates

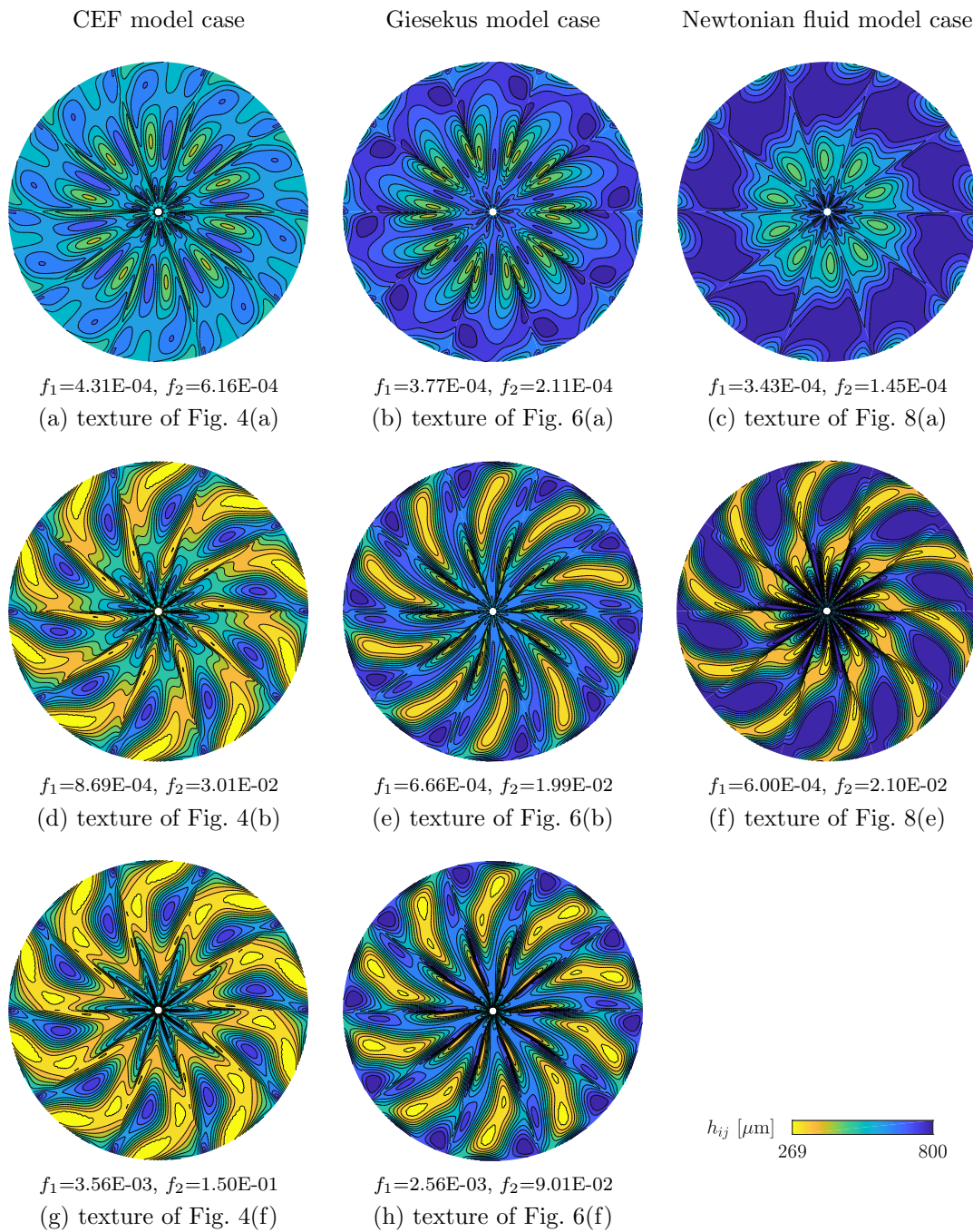


**Figure 10. Sample textured disc designs in the Pareto set from all three fluid model cases.**

that normal forces higher than what was purely achievable through only texture design depends solely on viscoelasticity. Further design studies using sequential design strategies (texture design optimization followed by fluid design, or vice versa) rather than simultaneous may provide stronger evidence for the effects of viscoelasticity on normal force generation.

As described in Sect. IV.D.2, each simultaneous texture and fluid design study (cases 1 and 2) used the same design objectives and variables. In other words, they involve the same design formulation, but use different numerical simulation approaches for prediction. Thus, unless two different solution sets provide the exact same objective function values, one of these two set of solutions may dominate the other. However, it is possible that multiple solutions exhibit with almost identical performance values. This issue is connected to the question of which fluid model or fluid solver can predict the behavior more accurately. A cross-validation

of one solution with different fluid models, as well as an experimental validation of the solution, is needed and is a topic of ongoing work.

#### IV.D.4. A Plan for Experimentation

A comprehensive comparison between numerical simulation results of the optimized texture and fluid and experimental results is planned. Preparation for the experimental measurement requires: *i*) fabrication of textured discs using additive (e.g., stereolithography, SLA) or subtractive (micro-milling) manufacturing, and *ii*) a fabrication of viscoelastic lubricants using a polyisobutylene (PIB) solution. These tasks remains as future work. Observing that all the design solutions on the Pareto frontier have different fluid properties, we will select carefully a set of sample designs to compare with simulation results.

## V. Conclusion

In this study, we designed the non-Newtonian lubricant properties and surface texture simultaneously for lubricated sliding contact using the MO-ASMO algorithm. The objectives of this design problem are: *i*) to minimize power input to reduce frictional loss, and *ii*) to maximize normal force to enhance load supporting capacity. We used two non-Newtonian fluid models—a modified Reynolds equation with the CEF model, and a Cauchy momentum equation with a multi-mode Giesekus model—to simulate nonlinear viscoelasticity in the flow field.

We obtained non-dominated optimal design solutions (i.e., Pareto sets), and compared a set of sample texture and fluid design results. Trends in texture shapes agreed with trends from our previous studies, and we also observed fluid parameter trends and how fluid design influences objective function values.

Our MO-ASMO algorithm was applied successfully to solve this simultaneous fluid and texture design problem with two objectives. Specifically, for the design problem using the Giesekus model, we solved the transient Cauchy momentum equations. A direct optimization (using either nonlinear programming (NLP) algorithms or genetic algorithms) was impractical given our computational resources. MO-ASMO enables solution without requiring access to exceptional high-performance computing resources. A specific challenge arises when attempting to use general-purpose NLP algorithms due to Giesekus model stability properties. Certain combinations of texture shape and fluid parameter values cause model divergence. An explicit and precise description of the boundary between compatible and incompatible parameter values is not available, making direct application of standard NLP solvers impractical. MO-ASMO mitigates these issues effectively using an SVDD strategy for adaptively constructing an explicit boundary between regions with acceptable input values and those that lead to divergence.

A topic of ongoing work is a comprehensive set of physical experiments to compare performance indices (power input and normal force) for a carefully-selected set of optimal texture and fluid designs. Texture fabrication, fluid fabrication, and experimental measurement are outside the scope of this article focused on optimization studies, and are identified as future work.

## Acknowledgments

This work was supported by the National Science Foundation under Grant No. CMMI-1463203. The authors also gratefully acknowledge support from the Procter & Gamble Company. In addition, we would like to thank our colleague Albert Patterson for assistance with our efforts toward physical experimentation, specifically texture fabrication methods.

## References

- <sup>1</sup>Wakuda, M., Yamauchi, Y., Kanzaki, S., and Yasuda, Y., “Effect of Surface Texturing on Friction Reduction Between Ceramic and Steel Materials Under Lubricated Sliding Contact,” *Wear*, Vol. 254, No. 3–4, 2003, pp. 356–363.
- <sup>2</sup>Etsion, I., “Improving Tribological Performance of Mechanical Components by Laser Surface Texturing,” *Tribology Letters*, Vol. 17, No. 4, 2004, pp. 733–737.
- <sup>3</sup>Johnston, M. T., King, W. P., and Ewoldt, R. H., “Shear Stress Characteristics of Microtextured Surfaces in Gap-Controlled Hydrodynamic Lubrication,” *Tribology International*, Vol. 82, 2015, pp. 123–132.
- <sup>4</sup>Lee, Y. H., Schuh, J. K., Ewoldt, R. H., and Allison, J. T., “Enhancing Full-Film Lubrication Performance Via Arbitrary Surface Texture Design,” *Journal of Mechanical Design*, Vol. 139, No. 5, 2017, pp. 053401–1–13.

<sup>5</sup>Schuh, J. K., Lee, Y. H., Allison, J. T., and Ewoltdt, R. H., "Design-Driven Modeling of Surface-Textured Full-Film Lubricated Sliding: Validation and Rationale of Nonstandard Thrust Observations," *Tribology Letters*, Vol. 65, No. 2, 2017, pp. 35–1–17.

<sup>6</sup>Schuh, J. K., *Surface Textures and Non-Newtonian Fluids for Decreased Friction in Full Film Lubrication*, Master's thesis, University of Illinois at Urbana-Champaign, 2015.

<sup>7</sup>Schuh, J. K., Lee, Y. H., Allison, J. T., and Ewoltdt, R. H., "Surface Textures and Non-Newtonian Fluids for Decreasing Friction in Lubricated Sliding Contact," *2015 Fluid Power Innovation and Research Conference*, Minneapolis, MN, 2015.

<sup>8</sup>Ashmore, J., Shen, A. Q., Kavehpour, H. P., Stone, H. A., and McKinley, G. H., "Coating Flows of Non-Newtonian Fluids: Weakly and Strongly Elastic Limits," *Journal of Engineering Math*, Vol. 60, No. 1, 2008, pp. 17–41.

<sup>9</sup>Lin, C., Lee, Y. H., Schuh, J. K., Ewoltdt, R. H., and Allison, J. T., "Efficient Optimal Surface Texture Design Using Linearization," *Advances in Structural and Multidisciplinary Optimization: Proceedings of the 12th World Congress of Structural and Multidisciplinary Optimization (WCSMO12)*, edited by A. Schumacher, T. Vietor, S. Fiebig, K. U. Bletzinger, and K. Maute, Springer, Cham, 2018, pp. 632–647.

<sup>10</sup>Lee, Y. H., Corman, R. E., Ewoltdt, R. H., and Allison, J. T., "A Multiobjective Adaptive Surrogate Modeling-Based Optimization (MO-ASMO) Framework Using Efficient Sampling Strategies," *Proceedings of the ASME 2017 IDETC/CIE Conference, Vol 2B: 43rd Design Automation Conference*, No. DETC2017-67541, Cleveland, OH, USA, Aug. 2017, p. V02BT03A023.

<sup>11</sup>Criminale Jr., W. O., Ericksen, J. L., and Filbey Jr., G. L., "Steady Shear Flow of Non-Newtonian Fluids," *Archive for Rational Mechanics and Analysis*, Vol. 1, No. 1, 1957, pp. 410–417.

<sup>12</sup>Bird, R. B., Armstrong, R. C., and Hassager, O., *Dynamics of Polymeric Liquids*, Vol. 1 Fluid Mechanics, Wiley, New York, NY, 2nd ed., 1987.

<sup>13</sup>Oldroyd, J. G., "On the Formulation of Rheological Equations of State," *Proceedings of the Royal Society A: Mathematical, Physical, and Engineering Sciences*, Vol. 200, No. 1063, 1950, pp. 523–541.

<sup>14</sup>Macosko, C. W., *Rheology: Principles, Measurements, and Applications*, Wiley, New York, NY, 1994.

<sup>15</sup>Owens, R. G. and Phillips, T. N., *Computational Rheology*, Imperial College Press, London, UK, 2002.

<sup>16</sup>Deville, M. O., Fischer, P. F., and Mund, E. H., *High-Order Methods for Incompressible Fluid Flow*, Cambridge University Press, Cambridge, UK, 2002.

<sup>17</sup>Kopriva, D. A., *Implementing Spectral Methods for Partial Differential Equations*, Springer, Netherlands, 2009.

<sup>18</sup>Keunings, R., "A Survey of Computational Rheology," *Proceedings of the XIIIth International Congress on Rheology*, 2000, pp. 7–14.

<sup>19</sup>Fornberg, B., *A Practical Guide to Pseudospectral Methods*, Cambridge University Press, Cambridge, 1996.

<sup>20</sup>Wang, G. G. and Shan, S., "Review of Metamodeling Techniques in Support of Engineering Design Optimization," *Journal of Mechanical Design*, Vol. 129, No. 4, 2007, pp. 370–380.

<sup>21</sup>Deb, K., Pratap, A., Agarwal, S., and Meyarivan, T., "A Fast and Elitist Multiobjective Genetic Algorithm: NSGA-II," *IEEE Transactions on Evolutionary Computation*, Vol. 6, No. 2, 2002, pp. 182–197.